Incorporating H-k Stacking with Monte Carlo Joint Inversion of Multiple Seismic Observables: A Case Study for the Northwestern US

Hanxiao Wu[1], Siyuan Sui[1], and Weisen Shen[1]

[1]Department of Geosciences, Stony Brook University, Stony Brook, New York 11794, USA

Corresponding author: Weisen Shen (weisen.shen@stonybrook.edu)

Key Points:

- We developed a new joint inversion approach that incorporates stacking of receiver function multiple phases with multiple data sets.
- The new approach reduces the trade-offs and improves the determination of deep crustal shear velocity, Moho, and Poisson's ratio.
- Application of the new method to the northwestern US produces a more accurate model that exhibits geologically coherent structures.

Keywords:

Tomography; continental crust; joint inversion; surface waves; receiver functions; H-κ stacking.

Abstract

Accurately determining the seismic structure of the deep crust of continents is crucial for understanding the geological record and continental dynamics. However, traditional surface wave methods often face challenges in solving the trade-offs between elastic parameters and discontinuities. In this work, we present a new approach that combines two established inversion techniques, receiver function H-κ stacking and joint inversion of surface wave dispersion and receiver function waveforms, within a Bayesian Monte Carlo (MC) framework to address these challenges. As demonstrated by the synthetic test, the new method greatly reduces trade-offs between critical parameters, such as the deep crustal Vs, Moho depth, and crustal Vp/Vs ratio. This eliminates the need for assumptions regarding crustal Vp/Vs ratios in joint inversion, leading to a more accurate outcome. Furthermore, it improves the precision of the upper mantle velocity structure by reducing its trade-off with Moho depth. Additional notes on the sources of bias in the results are also included. Application of the new approach to USArray stations in the Northwestern US reveals consistency with previous studies and also identifies new features. Notably, we find elevated Vp/Vs ratios in the crystalline crust of regions such as coastal Oregon, suggesting potential mafic composition or fluid presence. Shallower Moho depth in the Basin and Range indicates reduced crustal support to the topography. The uppermost mantle Vs, averaging 5 km below Moho, aligns well with the Pn-derived Moho temperature map, offering the potential of using Vs as an additional constraint to Moho temperature and crustal thermal properties.

Plain Language Summary

Knowing the seismic structure of the deep crust can help us understand Earth's geological history and how continents evolve. However traditional methods of studying the deep crust face challenges due to tradeoffs that can impact accuracies of the results. In this paper, we present a new approach that combines two existing techniques intending to measure the deep crust more accurately. We tested this method using both simulations and real data and found that it works better than previous methods. We applied this method to the Northwestern US and found that the results aligned with the area's geology, suggesting that the new method is feasible to be applied on a regional scale. The new method provides a more accurate way to study the deep crust and improves the mapping of the uppermost mantle.

1 Introduction

The seismic properties of the continental deep crust are critical to the understanding of the geological history and dynamic processes of the continents. For instance, the depth from the surface to the lower boundary of the crust, i.e., Moho depth, determines the 1st-order variations in surface topography through isostasy (e.g., Schmandt et al., 2015). Seismic velocities of deep crust are often used to infer the magma distributions, or compositional and thermal anomalies (Hacker et al., 2015a; He et al., 2021; Schmandt et al., 2019); Crustal Poisson's ratio, the elastic property related to the ratio between velocities of P and S waves (Vp/Vs), is often associated with the amount of the quartz, a key mineral that dominates the strength and deformation of the lithosphere (Lowry & Pérez-Gussinyé, 2011). As a result, the deep crustal properties such as Moho, velocity, and Vp/Vs have been extensively studied using large-scale seismic arrays, for example, USArray (e.g., Ma & Lowry, 2017; Shen & Ritzwoller, 2016; Sui et al., 2022). Extracting information about the Moho and Vp/Vs ratios is commonly done by analyzing P-wave-converted phases in receiver function (RF) waveforms (Ammon et al., 1990; Langston, 1977). Zhu & Kanamori (2000) proposed a simple method that employs a grid search in the Moho depth and Vp/Vs space (H-κ) to maximize the stacked amplitude of the P-s phase and the following multiple conversions (i.e., PpPs and PpSs+PsPs, Moho-multiples hereafter) in RFs from different events. Thanks to its simplicity, this method quickly gained popularity and has been applied globally, but its dependence on a priori absolute Vs value introduces potential bias in the derived results. On the other hand, surface waves, especially with the development of the ambient noise technique over the past two decades, have proven useful in constraining crustal velocity structure (Ritzwoller et al., 2011) as Rayleigh waves are sensitive to absolute velocity. With the complementary sensitivities of RF and surface waves, the two observables are often combined to infer both absolute velocity and Moho depth (e.g., Juliá et al., 2000; Shen, et al., 2013b). However, the determination of crustal Vp/Vs ratios in such joint inversions using RF waveforms is challenging, as 1)the P-s phase alone cannot solve the trade-off between Moho depth and crustal Vp/Vs; 2) wiggles of the Moho-multiples are either too weak to be directly inverted due to low signal-to-noise ratios or are often obscured by sediments reverberations (Yu et al., 2015); 3) processing like harmonic stripping of RFs to obtain the averaged waveform further suppressed Moho-multiples. As a result, additional pre-processing is usually required to increase the signal-noise ratio (Chen & Niu, 2013) or to remove sediments-reverberations (Yu et al., 2015). Consequently, the Moho-multiples are often not used in the joint inversion with RF waveforms (Shen, et al., 2013b), leaving crustal Vp/Vs poorly constrained and can only be presumed during the inversion (e.g., Juliá et al., 2000). As crustal Vp/Vs trades off with other parameters, it results in insufficient constraints on all parameters of interest. An example of this

outcome for joint inversion is highlighted in Fig. 1a, which presents this trade-off based on the result of a synthetic test when crustal Vp/Vs is treated as a free parameter. In this test, we only accept models that fit surface wave dispersion and receiver function waveform that contains only the Moho P-s phase. The scatter plot in Fig. 1a shows two crustal parameters, Moho depth and lowermost crustal Vs (defined as the averaged Vs within 5 km above Moho) from the accepted models. When considering crustal Vp/Vs ranging from 1.6 to 1.9 (typical for crustal rocks), the resulting models exhibit considerable variation in lowermost crustal Vs values, ranging approximately from 3.4 to 4.2 km/s which spans nearly all common lower crustal lithologies (Hacker et al., 2015a). They leave the true uncertainties in Moho depth ~ 4-5 km, underscoring the limitations of existing joint inversion methods in effectively constraining these parameters without knowing the accurate crustal Vp/Vs value.

In this study, we propose a new approach that combines the widely used H-κ stacking method with the joint inversion of RF waveforms and surface wave dispersion within a Bayesian Monte Carlo (MC) sampling algorithm, aiming to simultaneously solve the trade-offs mentioned above. Also shown in Figure 1a, although a broad range of models can fit the dispersion curves and RF waveform, only a subset of models exhibits sufficiently high stacked H-κ energy of the three major Moho-converted phases (i.e., Ps, PpPs, and PpSs+PsPs). This demonstrates that if we incorporate H-κ stacked energy into the joint inversion framework, it is possible to resolve the trade-offs among all three parameters simultaneously. Notably, we outline this new method and demonstrate its feasibility through a comprehensive synthetic test in Section 2. Additionally in Section 3, we apply the new technique to investigate the deep crustal structure in the Northwestern United States, which features diverse geological settings, allowing us to assess the method's effectiveness in characterizing various crustal structures. The area has been investigated intensively in the past decade, providing benchmarks for the results to be compared. In Section 4, we discuss the errors associated with the method and present the new features in the resulting 3-D model. We particularly show how our approach additionally improves the understanding of the uppermost mantle structure. Caveats and potential improvement of the method is also included in this Section. We end the paper with a concise summary. We also discuss the shortcomings of this method and where improvements are worthwhile.

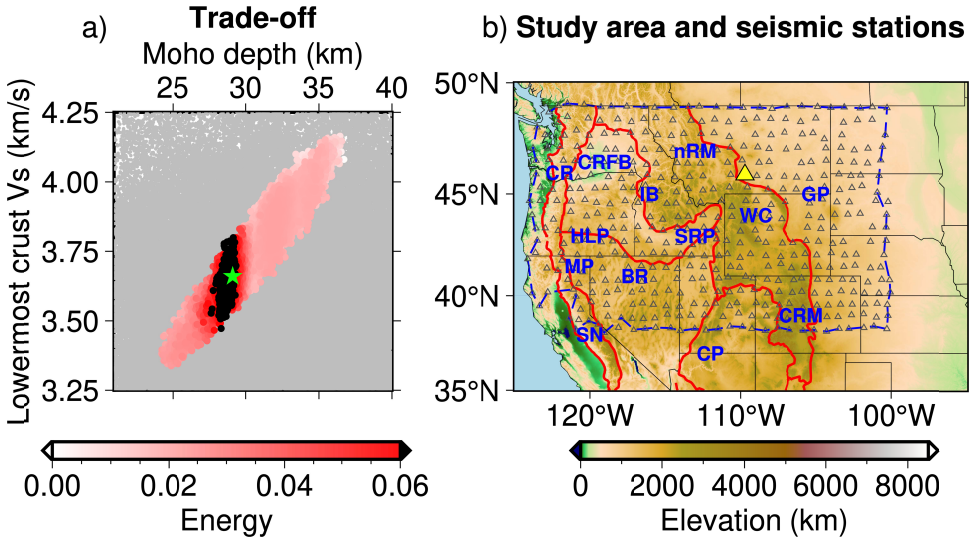

Figure 1. a) Trade-off between Moho depth and lowermost crust Vs (averaged within 5 km above Moho) observed in a joint inversion of surface wave dispersion and receiver function waveform (Shen, et al., 2013b) based on a synthetic model. In this inversion, the bulk Vp/Vs of the crystalline crust is set as a free parameter. Prior sampling models are plotted as the background in gray color, on top of which are the accepted models from the Monte Carlo search, color-coded by their H-κ stacked energy. The true value of the target model is marked by a green star. **b**) Stations of the EarthScope USArray/Transportable Array (TA) used in this study are shown with triangles. The main geological provinces are outlined with red contours (ref). Station F18A, which is used as an example to demonstrate the new method, is marked by a yellow triangle. The blue dashed line outlines the studied area for which a final 3-D crustal and uppermost mantle model is made. Physiographic locations in the study are identified with abbreviations: Snake River Plain (SRP), Cascade Range (CR), Columbia River Flood Basalts (CRFB), Idaho Batholith (IB), Basin and Range (BR), High Lava Plains (HLP), Modoc Plateau (MP), Great Plains (GP), Colorado Rocky Mountains (CRM), Colorado Plateau (CP), Wyoming Craton (WC), Sierra Nevada (SN), and northern Rocky Mountains (nRM).

2 Methods

During the new inversion process, we aim to determine a one-dimensional (1-D) seismic structure beneath each station location that effectively fits the seismic data. The 1-D model employed in this study follows the methodology proposed by Shen et al. (2013b), which characterizes the shallow Earth as comprising three layers: a sedimentary layer, a crystalline crustal layer, and an uppermost mantle layer. Each layer is defined by a depth-dependent Vs profile and is separated by discontinuities at the base of sediment and Moho. The density and Vp profiles are derived from the Vs profiles. For the sedimentary layer, density, and Vp/Vs values are scaled using empirical relationships established by Brocher (2005). The density scaling for the uppermost mantle layer is determined using the empirical relationship introduced by Hacker & Abers (2004), while the Vp/Vs ratio for the uppermost mantle is fixed at a value of 1.789. In contrast to previous joint inversion studies, where the crystalline crustal Vp/Vs was either held constant (e.g., Shen, et al., 2013a) or scaled from Vs (e.g., Yang et al., 2020), our approach treated it as a free parameter that ranges from 1.55 to 1.95 (see Table.S1 in Supplementary Material for more information about model parameterization). Furthermore, we impose predetermined rules or boundary conditions to constrain the model space (see Table.S2 in Supplemental Material for more details). Specifically, prior constraints are established to ensure that velocity and density exhibit positive jumps across the discontinuities.

2.1 Monte Carlo Sampling

In order to incorporate the H-κ stacked energy as part of the Bayesian framework, we also modify the MC search. In a Bayesian MC framework, the posterior distribution σ(m) is related to the prior distribution ρ(m) through likelihood function L of any given model m:

$$\sigma(m) \propto \rho(m)L(m) \qquad (1)$$

To sample the posterior distribution, we created the MC chain following the flowchart in Fig. 2. In this chain, a new model (m_{new}) is generated based on the last accepted model (m_{old}) and is

accepted or rejected according to a chance p which is determined by comparing its likelihood $L(m_{new})$ to the likelihood of the last accepted model ($L(m_{old})$). For joint inversion of surface wave dispersion and receiver function waveforms, likelihood ($L^S(m)$) is defined based on the misfit $S(m)$ between the predicted $d(m)$ and observed data d^{obs}:

$$L^S(m) = exp\left(-0.5S(m)\right) \qquad (2)$$

where

$$S(m) = (d(m) - d^{obs})^T C_e^{-1}(d(m) - d^{obs}) \qquad (3)$$

In the new approach, we further defined an additional likelihood function for the H-κ stacked energy for each newly generated model:

$$L^E(m) = exp\left(E^n(m)\right)^a \qquad (4)$$

Where the E^n represents the normalized stacked energy of predicted *Ps*, *PpPs*, and *PsPs+PpSs* phases for all usable teleseismic events:

$$E^n(m) = \frac{1}{N * E^{ref}\,\sout{(m)}} \sum_{i=0}^{N} w_1 RF^{[i]}\left(t_{Ps}^{[i]}(m)\right) + w_2 RF^{[i]}\left(t_{PpPs}^{[i]}(m)\right) - w_3 RF^{[i]}\left(t_{PsPs+PpSs}^{[i]}(m)\right). \qquad (5)$$

Where w_k(k=1,2,3) are the weighting of Ps, $PpPs$, and $PsPs + PpSs$ phases and are empirically set to be 0.3, 0.4, and 0.3 in this study, respectively. N is the number of RF waveforms that are stacked. The E^{ref} is a reference energy that is used to normalize stacked energy to be mostly between 0 and 1. An ad-hoc factor a is empirically set so that the MC search is guided toward maximizing the H-□ stacked energy at a similar rate of fitting other data. $t_{Ps}(m)$, $t_{PpPs}(m)$, and $t_{PsPs+PpSs}(m)$ are the arrival time of Ps, $PpPs$, and $PsPs + PpSs$ phases, predicted based on model m, respectively. In traditional H-κ stacking introduced by Zhu & Kanamori (2000), the arrival time is calculated based on a simple two-layer model, involving only the thickness (i.e., Moho depth) and velocity of the upper layer (i.e., crust). Later, Yeck et al. (2013) developed the sequential H-κ stacking method based on this foundation. They separated the sedimentary layer from the crust and constructed a three-layer model (sedimentary layer, crystalline crust layer, and mantle layer). The calculation of arrival times in Yeck's approach involves the thickness and velocity of both the sedimentary and crystalline crust layers. Although our model is also divided into three basic layers (sedimentary layer, crystalline crust layer, and mantle layer; see Table.S1 model parameterization in Supplemental material), each basic layer, in fact, consists of a more refined 1-D velocity profile (as shown in Fig.3a). Therefore, our arrival time calculations differ slightly from traditional H-κ stacking, as shown below:

$$t_{Ps}(m) = \sum_{k=1}^{l} h_k(m) \times \left(\sqrt{\frac{1}{V_{k,s}^2(m)} - p^2} - \sqrt{\frac{1}{V_{k,p}^2(m)} - p^2} \right) \qquad (6)$$

$$t_{PpPs}(m) = \sum_{k=1}^{l} h_k(m) \times \left(\sqrt{\frac{1}{V_{k,s}^2(m)} - p^2} + \sqrt{\frac{1}{V_{k,p}^2(m)} - p^2} \right) \quad (7)$$

$$t_{PsPs+PpSs}(m) = \sum_{k=1}^{l} 2h_k(m) \times \left(\sqrt{\frac{1}{V_{k,s}^2(m)} - p^2} \right) \quad (8)$$

Where l is the number of layers above the Moho, while h_k,$V_{k,s}$, and $V_{k,p}$ denote the thickness, Vs, and Vp of the k-th layer, respectively.

As an iterative approach, MC inversion needs an initial model to begin the iteration. In each round of MC sampling, the initial model is independently randomly generated within the model space. For each inversion, we perform 30 rounds of sampling, with each sampling iterating 8000 times. This means that one inversion generates 240,000 models (including all accepted and rejected ones). After the whole search (30 rounds of sampling) is complete, we perform several post-processing operations, including:

1) Removing certain models. Near the beginning of the sampling, a few models are accepted before they enter the equilibrium state, so these models should be discarded based on their high misfit to dispersion, receiver function waveforms, and low H-κ stacked energy.

2) Calculate the average of the accepted model ensemble which defines the final inverted model.

3) Calculate the standard deviation of the ensemble.

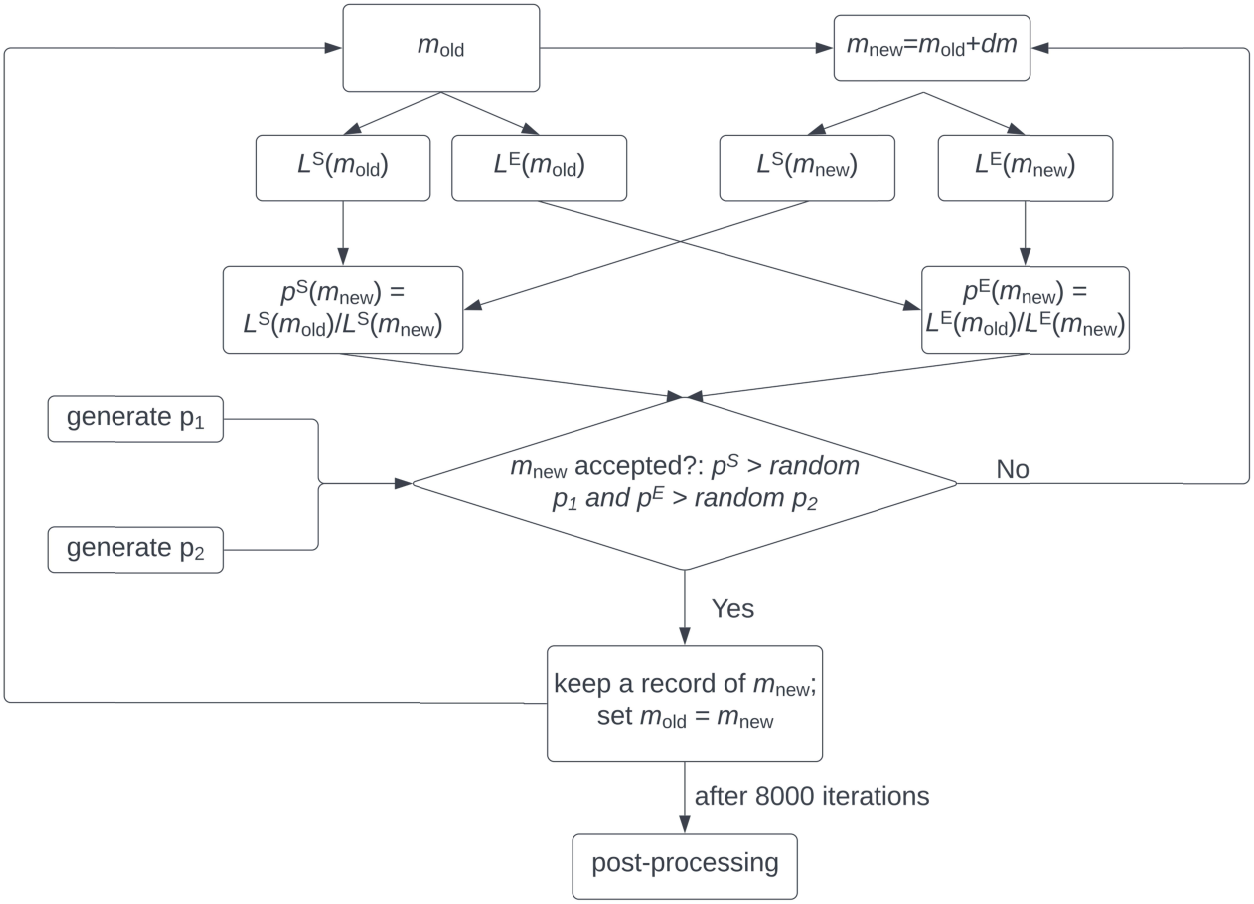

194

195 **Figure. 2.** A flowchart of the new joint MC sampling incorporating H-κ stacking. $L^S(m)$ and
196 $L^E(m)$ are likelihood functions associated with the misfit and the H-κ energy, respectively. p^S
197 and p^E are the probabilities of being accepted according to misfit-related likelihood and the H-κ
198 energy-related likelihood, respectively. The acceptance is determined by comparing p^S and p^E
199 with randomly generated numbers between 0 and 1 (i.e., p_1 and p_2) These two numbers are
200 independently randomly generated in every iteration. The process highlighted here begins after
201 an initial model is generated, and 'post-processing' begins after samplings are performed on 30
202 different initial models.

203 2.2 Synthetic test

204 In our study, we conducted a synthetic test to evaluate the performance of the proposed
205 approach. A target model is designed as shown by the red lines in Fig. 3a (labeled as 'target'),
206 and the proposed approach is applied to the data generated based on this target model. This target
207 model features a monotonically increasing crustal Vp/Vs ratio with a bulk value of ~ 1.74, a
208 crustal thickness of ~ 29 km, and an average lowermost crustal Vs of ~ 3.66 km/s. The synthetic
209 datasets, including ~200 RF waveforms with different ray parameters for H-k stacking (Fig.3b),
210 surface wave dispersion (Fig.3c), and the first 10-sec RF waveform (Fig. 3d) with a ray
211 parameter of 0.06s/km. All data are added by normally distributed random noise based on real
212 practice (see Table.S2 in Supplemental Material for more information about noise level). When

applied to real data, individual RFs will be the raw RF waveforms generated by individual events, and the first 10-sec RF waveform will be the representative RF that is slowness corrected and azimuthally averaged from all events (e.g., Shen, et al., 2013b).

Fig.3 and Fig.4 present the results of the synthetic test. The ensemble average (blue line, labeled as 'inverted') of the Vs model, which is considered as the final inverted model, closely resembles the target model and well predicts the arrivals of Moho-converted phases, group and phase velocities, and RF waveforms (Fig.3b-d). Please note that in our target model configuration, the Vp/Vs ratio of the crystalline crust is not a uniform value but varies with depth (Fig.S1b) with a bulk value of ~1.741. However, during the MC inversion, the Vp/Vs ratio of the crystalline crust is perturbed and inverted as a single value. In other words, this new approach aims to obtain the bulk Vp/Vs ratio of the crystalline crust, instead of a fine 1-D Vp/Vs structure. Consequently, in theory, the Vp structure cannot be accurately resolved (Fig.3a). Using the new approach, the trade-offs between lowermost crust Vs, Moho depth, and crustal Vp/Vs are greatly reduced (Fig.4d-f), leading to more precise results close to the true values of the target model (Fig.4a-c). This test demonstrates the feasibility of the proposed approach when applied to synthetic data. We note that a small bias in Moho depth is observed, and this will be discussed with more detail in Section 4.1.

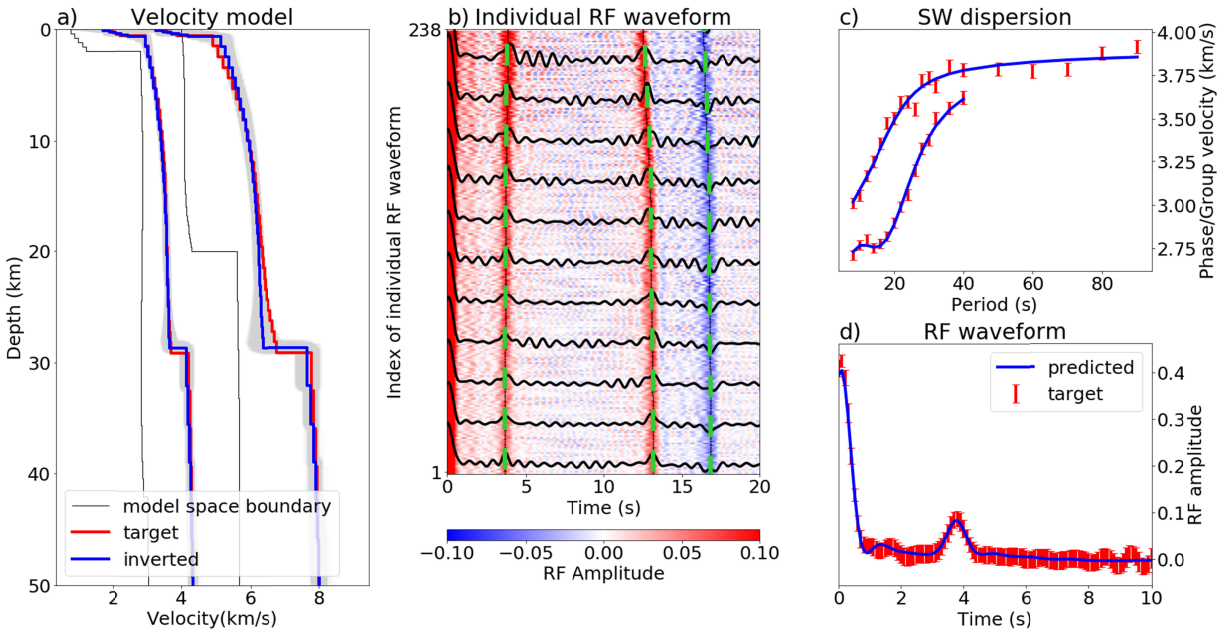

Figure 3. Inversion result of the synthetic test. **a**) S-wave and P-wave velocity models. The target model (red lines, the model we used to generate the synthetic data) and the inverted model ensemble (grey profiles) that was accepted by the MC sampling are presented, and the average of the accepted model ensemble is shown by the blue lines, for both P and S wave profiles. The model space for Vs is highlighted by two thin profiles. **b**) Data fitting to the H-κ stacked energy. The black wiggles are examples of RF waveforms with small vertical green bars that denote the predicted arrival time for the Moho-converted phases (e.g., Ps, PpPs, and PpSs+PsPs phase) based on the inverted model (blue lines in Fig 3a). All receiver function data involved in the inversion is plotted as colored backgrounds and indexed according to their slowness. **c-d**) Data

fitting to surface wave dispersion and RF waveform. The red bars represent the synthetic data (generated from the target model) with normally distributed random noise added. The blue lines denote the data predicted by the inverted model (blue lines in panel a).

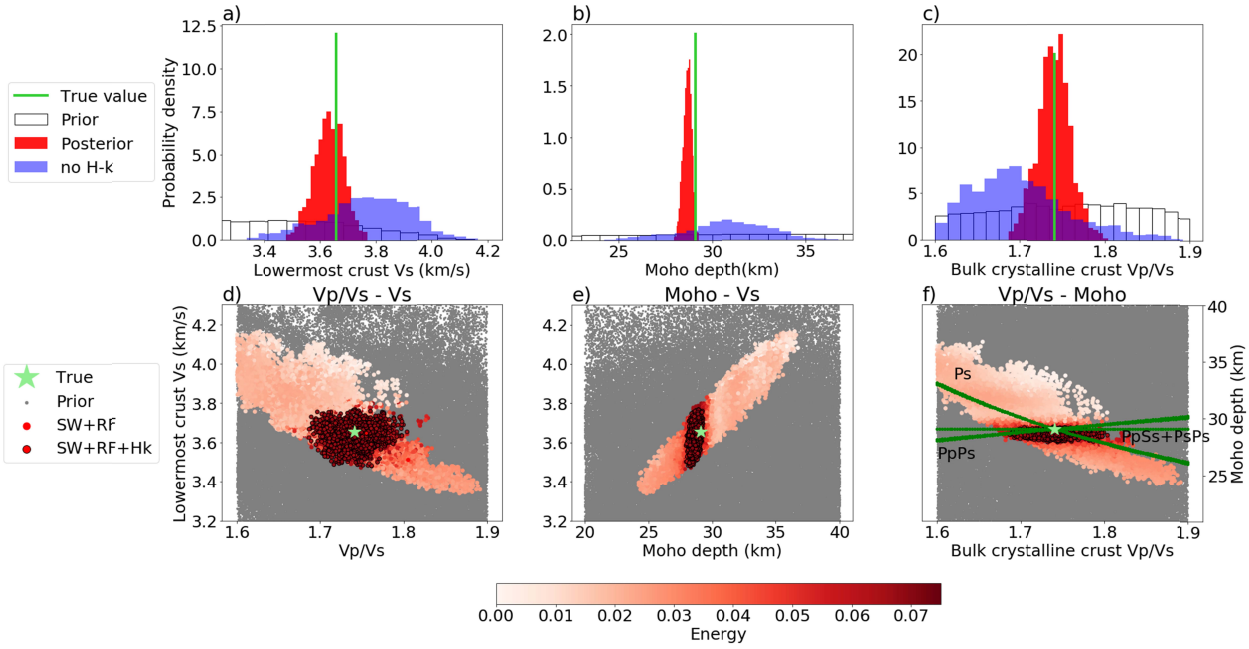

Figure 4. a–c) Prior and posterior distribution of lowermost crust Vs, Moho depth, and crystalline crust Vp/Vs. Prior distributions are plotted as background in white histograms. Red histograms represent the posterior distribution generated by the new approach which uses surface wave dispersion, RF waveform, and H-κ stacked energy. Blue histograms represent the posterior distribution generated by traditional joint inversion which only uses SW dispersion and RF waveform. The true value of each parameter is marked by the green vertical lines. **d**) Trade-off between the lowermost crust Vs and bulk crystalline crust Vp/Vs. Each reddish dot represents an accepted model, color-coded by its stacked H-κ energy. The results of the traditional joint MC inversion are marked by open dots color-coded by their H-κ stacked energy. The results of the new joint inversion are marked by closed dots, also color-coded by the corresponding H-κ stacked energy. The green stars represent the true values of the target model. **e)** Similar to d, but for the trade-off between the Moho depth and lowermost crust Vs. f) Similar to Fig d, but for the trade-off between the crystalline crust Vp/Vs and Moho depth. The dark green lines represent the theoretical H-κ relations between Moho depth and bulk crystalline crust Vp/Vs for different Moho-converted phases (Zhu & Kanamori, 2000).

3 Applying the new method to Northwestern US

To demonstrate the feasibility of our new approach to real data, we applied it to ~ 450 USArray stations in the northwestern US (Fig.1b), where the region has been extensively studied using both H-κ stacking (Eagar et al., 2011) and surface wave-RF joint inversions (Delph et al., 2018; Shen, et al., 2013a). The Rayleigh wave dispersion curves and representative RF waveforms with uncertainties are collected from Shen & Ritzwoller, (2016), and the individual raw RF waveforms are collected from Sui et al. (2022). The frequency content of individual RFs used for

H-κ stacking was chosen by the common choice of the Gaussian parameter of 2.5 (centered around 1 sec). The RFs are computed from three-component seismograms using a time-domain iterative deconvolution method (Ligorría & Ammon, 1999) and then undergo a 5-stage quality control which removes the poor-quality data (Sui et al., 2022) After the rigorous quality control scheme by Sui et al., (2022), this station retained 47 high-quality RF waveforms that can be used to calculate H-κ stacked energy during the MC inversion.

Fig.5 shows the inversion result of an example station F18A, which is in Big Timber, MT, off the Rocky Mountain front range. As shown in Fig. 5b, three major Moho-converted phases (i.e., Ps, PpPs, PsPs+PpSs) can be identified in the RF waveforms. The joint MC inversion yielded ~ 6000 1-D models, and their average model successfully predicts the arrival times of Moho-converted phases (Fig. 5b), while simultaneously fitting the dispersion and the representative RF waveform (Fig. 5c-d). The posterior marginal distribution shows significant reductions in uncertainty compared to the posterior distribution generated by the inversion without H-κ energy: the uncertainty in crustal Vp/Vs is reduced by ~ 71%; Moho depth uncertainty is reduced by 90%; and lowermost crust Vs uncertainty is also reduced by more than 50%.

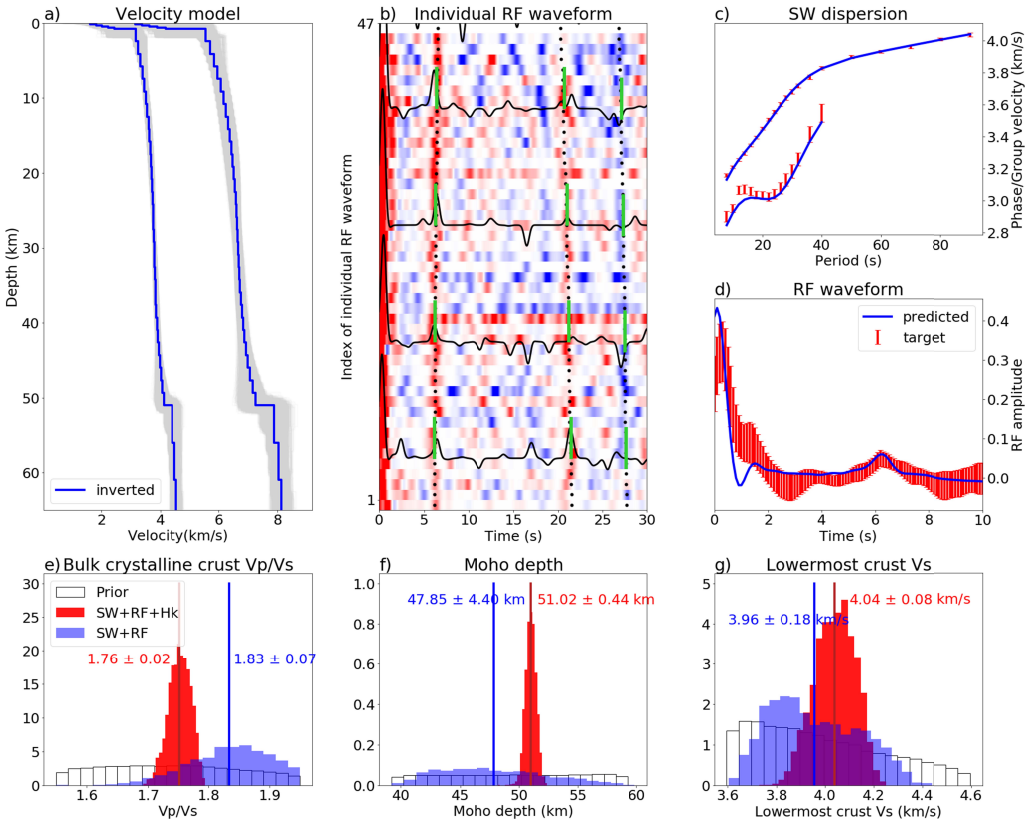

Figure 5. Result for USArray station F18A from the new approach. **a-d**) Similar to Fig.2a-d; **e-g**) Similar to Fig.3a-c. The red and blue vertical lines represent their respective mean, with the specific numerical values (mean +/- standard deviation) labeled next to them.

Out of the ~ 450 stations in the study region with all three data types, meaningful results were successfully produced for more than 70% of them, except for those in the Great Plains due to complications arising from the thick sedimentary cover that generates reverberations and masks

the Moho-converted phases that we aim to use. Those impacted stations often have higher misfit and low stacked energy and are not used for further analysis. The resulting 1-D models were then combined to form a 3-D seismic model for the crust and uppermost mantle. As this study focuses on how the combination of H-κ stacked energy helps constrain the deep crustal structures (including Moho), the presentation of the results is primarily focused on the corresponding parameters.

As shown in Fig 6, the Vp/Vs map reveals an average Vp/Vs value of ~ 1.77 for the crystalline crust, with variations highly correlated with tectonic boundaries. High Vp/Vs is found near the High Lava Plain (e.g., S. Oregon), which is also connected with relatively high Vp/Vs along the Snake River Plain. The most prominent low Vp/Vs is seen in southern Idaho, northern Oregon, and Washington, encompassing the Idaho Batholith and along the northern Cascades. Both the Moho depth map and lowermost crust Vs map exhibit a west-east dichotomy. The thinnest crust is observed in regions such as the Basin and Range and Columbia River Flood Basalts, while the thicker crust is observed in the Great Plains, Wyoming Craton, and Colorado Rocky Mountains. The western region exhibits lower velocities, except for a relatively higher velocity in the Columbia River Flood Basalt compared to its surroundings.

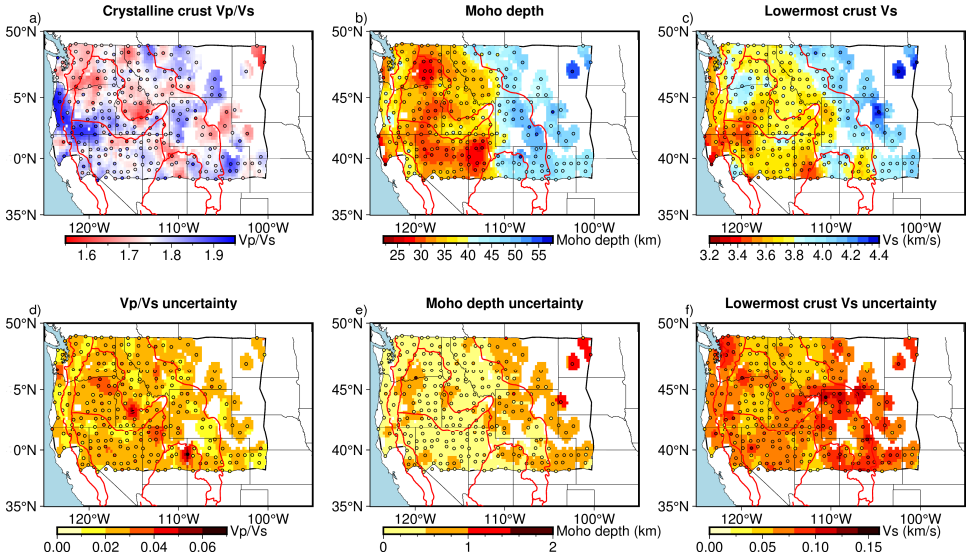

Figure 6. Crustal architecture of the NW US. derived from the new approach **a)** Bulk Vp/Vs of crystalline crust, **b)** Moho depth, and **c)** averaged Vs within 5 km above the Moho. **d-f)** Corresponding 1-standard deviation of the posterior distributions.

4 Discussion and conclusion

4.1 Systematic errors

Model errors include systematic and nonsystematic errors. The nonsystematic errors should encompass model fluctuations and will be controlled predominantly by errors in the data and trade-offs between model parameters at different depths **(**Shen & Ritzwoller, 2016) Specifically, our method yields average uncertainties (1-sigma) in crustal thickness of ~ 0.5 km (Fig. 4c), representing a substantial improvement over previous joint inversion results that did not involve

H-κ stacked energy (e.g., Shen, et al., 2013a) , with uncertainties of ~4 km). This improvement can be attributed to including PpPs and PsPs+PpSs phases in the inversion process. Furthermore, the more precise determination of Moho depth reduces the uncertainties in the lowermost crustal Vs to ~0.07 km/s, a 30% reduction compared to the uncertainties reported by Shen, et al. (2013a) (~0.1 km/s). In this section, we mainly discuss the systematic errors.

Systematic errors come from the assumptions and the method itself. Shen & Ritzwoller (2016) introduced the traditional MC joint inversion method, and they elucidated three pivotal factors linked to systematic errors, which are 1) the scaling of density from Vs; 2) the choice of Q in the mantle; and 3) the scaling relationship between Vp and Vs. Given that our approach is rooted in their method, it inherits these problems to some extent. Regarding the first two factors, Shen & Ritzwoller (2016) conducted an exhaustive discussion, thus obviating the necessity for further elaboration in this context. The third factor is that they were unable to constrain Vp/Vs, and therefore had to set it as a prior parameter. Our novel approach addresses this issue by incorporating H-κ energy into inversion. However, the inclusion of the H-κ data introduces yet another layer of systematic error. The MC inversion involves obtaining a set of models that can reasonably fit the data (i.e., with a misfit below a critical value and H-κ energy above a critical value) and then using their average as the final result, instead of selecting the model that fits the data 'best' (i.e., smallest misfit or highest energy). This strategy is employed due to the recognition that the presence of errors in the data can lead to an overfitting of the model to these errors when opting for the 'best-fitting' model. It is worth noting that as long as the errors in data are completely random and unbiased, this strategy itself should not introduce systematic errors.

However, some biases remain when H-κ energy is incorporated into the joint inversion. The essence of H-κ stacking is to fit the arrival times of different phases by searching for the model associated with the maximum energy. This operation relies on the underlying assumption that the maximum energy (amplitude) corresponds precisely to the true arrival time of each Moho-converted phase. However, this assumption does not always hold true. In instances where a thin low-velocity sedimentary layer is present (such as the target model in the Section 2.2 synthetic test), the Moho-converted phases (particularly the PpPs and PsPs+PpSs phases) may be contaminated by additional reverberations generated by other discontinuities (e.g., the bottom of sedimentary layer or/and velocity changes in the lower crust) given that individual phases are limited in frequency. This contamination to Moho converted phases causes the waveform distortion that shifts the maximum energy or generates an asymmetric phase (e.g., Fig. 7). Consequently, the maximum energy no longer coincides with the true arrival time, as shown in Fig.7g-i. As a result, the final inverted model becomes biased, manifesting as a shallower Moho or/and higher Vs (to generate shorter arrival times). It's worth noting that this systematic error primarily manifests in the estimates of Moho depth and Vs, with minimal impact on Vp/Vs – this can be observed in both the posterior distribution (Fig.4a-c) and the trade-off plots (Fig. 4d-f). This also aligns with the perspective presented in Zhu & Kanamori's paper for H-κ stacking (2000), which suggests that bias in Vs primarily affects the estimation of Moho depth with a lesser impact on Vp/Vs.

It can be noticed that in cases where the sedimentary layer is sufficiently thick, the issue of maximum energy shift no longer persists (Fig.7d-f). In such scenarios, the additional reverberations from near-surface structures will arrive later to the extent that they are separated from the Moho-converted phases. However, even in this circumstance, an asymmetry problem remains. In a simple two-layer model comprising a crust and a mantle layer with constant velocities, the shape of the Moho-converted phase is symmetric with respect to the theoretical arrival time (Fig.7a-c). However, when contaminated by additional reverberations, the Moho-converted phases are not symmetric anymore even though the arrival of the maximum energy might not be affected. As indicated in Fig.7d-f, the energy of the left side (associated with shorter travel times) of the PpPs and PpSs+PsPs phases is stronger than that on the right side (related to longer travel times). In such cases, the MC search will tend to favor the models that can predict shorter arrival times (manifested as higher Vs or/and thinner Moho), despite the maximum energy remaining aligned with the true arrival.

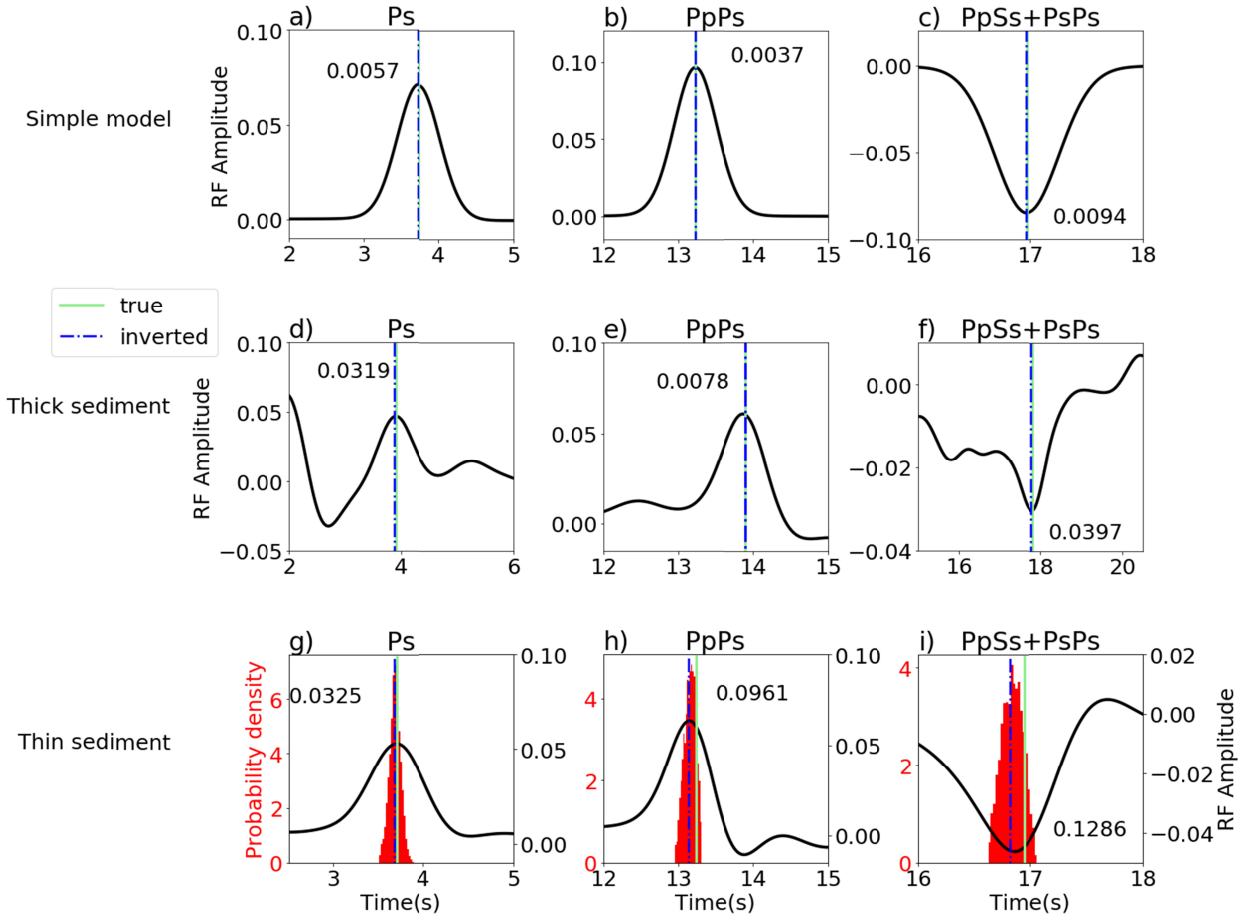

Figure 7. Noiseless synthetic RF waveforms with a ray parameter of 0.04 s/km. **a**) - **c**) Ps, PpPs, and PpSs+PsPs phases of RF waveform that are generated based on a simple two-layer model that consists of a 40-km-thick crust layer with Vs of 3.5 km/s and a 160-km-thick mantle layer with Vs of 4.3 km/s, respectively. **d**) - **f**) Similar to panels a-c, except that they are generated based on a more complex model with a thicker sediment layer (2.6km). **g**) - **i**) Similar to panels

d-f, except that they are generated based on the target model used in the synthetic test in Section 2.2, which has a thin sediment layer (0.6km). The green vertical bars represent the true arrival times of targeting Moho-converted phases (i.e., Ps, PpPs, and PpSs+PsPs), and the blue vertical bars represent the arrival times calculated based on the final inverted model. Note that the true arrival times of the Moho-converted phases do not correspond to the maximum energies in the waveform due to interference of other phases, especially in the case of thin sediments. The differences between the true (green) arrival times and inverted (blue) arrival times are labeled by black text (unit is sec) in each plot. The arrival times calculated based on each accepted model are plotted as the red background histograms in g-i. Note that phases based on the simple model are symmetric and the maximum energy corresponds to the theoretical arrivals of the Moho multiples. All three corresponding models can be found in supplemental materials (Fig.S2).

Assessed by the difference between the true arrival and the arrival predicted based on the inverted model, the bias introduced by the asymmetrical phases is significantly smaller than the bias introduced by the maximum energy shift. We also did the same synthetic test using the model with a thick sedimentary layer and the simple two-layer model, respectively (see Fig.S4 & Fig.S5 in the supplemental material for more information on inversion results). The noise level is set the same as it is in section 2.2. The difference between the true Moho depth and the inverted Moho depth is 0.43 km, and 0.17 km for the thin and thick sediment model tests, respectively. For the simple two-layer model, the test reveals a 0.13 km difference in Moho depth, probably from random noise we added to the data. The 1-sigma of the Moho depth is 0.23km for the test with a thin sediment model, ~ 50% of the systematic bias. This indicates that the potential systemic errors might exceed the random errors for certain stations with sedimentary cover and make the uncertainties presented underestimated.

4.2 Benchmark of the resulting model

The map views of the Vp/Vs from selective previous studies (Ma & Lowry, 2017; Sui et al., 2022 and EARS, the EarthScope Automated Receiver Survey, Crotwell & Owens, 2015, Trabant et al., 2012) are plotted in Fig.8 for comparison. It should be noted here that the Ma & Lowry, 2017 and EARS results are for the bulk crust, while our result and Sui et al. (2022) are for the crystalline crust. Over, the general variations in the Vp/Vs map are consistent, but the new result reveals more pronounced and geologically correlated variations (e.g., the contrast between the Snake River Plains and Idaho Batholith). The result from the EARS project is fully automatically generated using the classic H-κ stacking method. This automatic processing uses a less strict quality control scheme compared with other studies, generating a more mosaic map affected by the data noise. It also treats crust as a simple single-layer model, which also introduces bias due to the effects of the sedimentary layer (Yeck et al., 2013). Sui's result (Fig. 8b) is derived using sequential H-κ stacking (Yeck et al., 2013) which treats the sedimentary layer and crystalline crust separately. The sequential H-κ stacking reduces the influence of the sediment layer, and their map features very similar patterns to our result. The map from Ma & Lowry (2017) is obtained by a joint inversion of Bouguer gravity anomalies and seismic receiver functions. It is worth noting that the gravity data in that study are used to indirectly constrain the Vp/Vs, which depends on a general relationship between density and Vp/Vs. As crustal rocks vary, this

relationship may not hold true everywhere. Our study, in contrast, directly constrains the Vp/Vs and eliminates the need to assume such a Vs-density relationship, leaving gravity an independent metric for estimating density separately in the future. In addition, results from the three previous studies are subject to the assumption in crustal Vs or Vp, which may introduce biases and uncertainties. In comparison, our approach addresses these limitations by simultaneously constraining both the velocity structure and Vp/Vs ratio, resulting in a significant reduction in uncertainty and trade-offs.

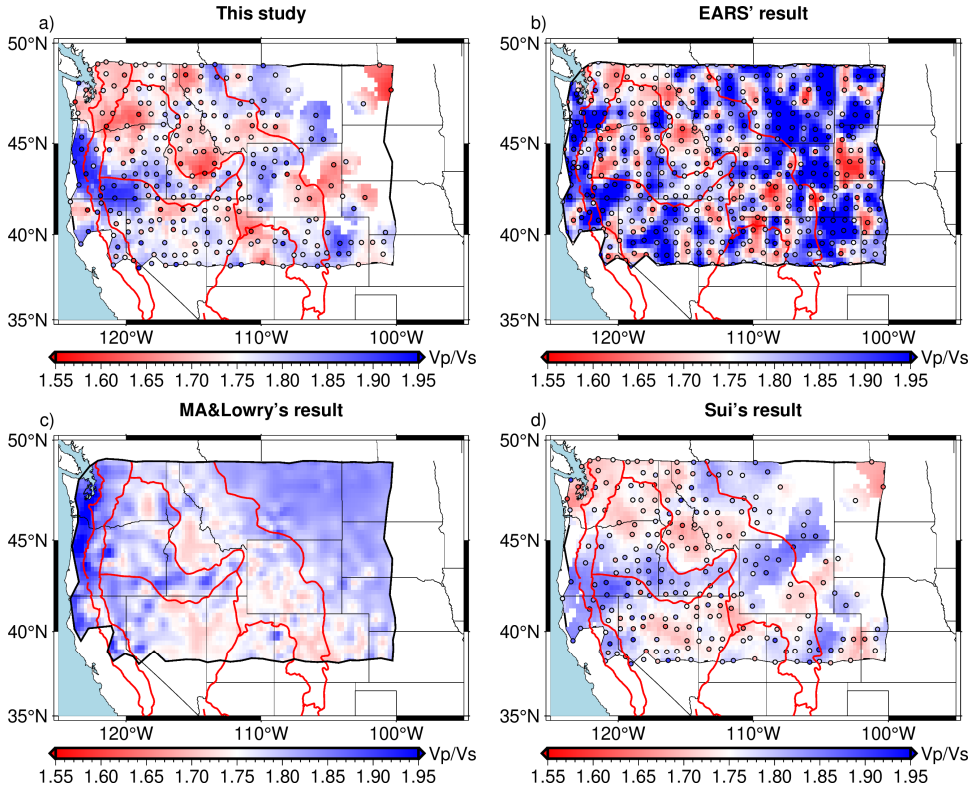

Figure 8. Comparison of Vp/Vs maps from different studies. **a**) Bulk Vp/Vs of crystalline crust obtained in this study. **b**) Bulk Vp/Vs of the crust (including both the sediment layer and crystalline crust) derived from the automatically processed H-k stacking (EARS, Crotwell et al., 2005, Trabant, et al., 2012). The Vp/Vs values are depicted using the same color scale to highlight the general consistency and differences in details from various approaches. **c**) Bulk Vp/Vs of the crust (including both the sediment layer and crystalline crust layer) constrained by RFs and gravity data (Ma & Lowry, 2017). **d**) Bulk Vp/Vs of crystalline crust derived through sequential H-κ stacking (Sui et al., 2022).

The map view of lowermost Vs and Moho depth of Shen & Ritzwoller's 2016 model (SR2016) are plotted in Fig.9 for comparison. The SR2016 model is obtained by the traditional MC inversion using surface wave data and the first 10-s averaged RF waveform, assuming the bulk Vp/Vs ratio of the crystalline crust is 1.75. Compared with the SR2016 model, the Moho depth is generally thinner, and it exhibits a stronger contrast in crustal thickness between the tectonically thinned (rifted) western United States and the stable central/eastern United States. For example, ~ 5 km thinner in the Basin and Range, Columbia River Flood Basalt, and High Lava Plain are

observed. It also indicates a discernible decrease in the lowermost crust Vs, with an average reduction of ~ 4% when compared with the SR2016 model, especially in regions like Modoc Plateau, and the boundary between Colorado Plateau and Basin and Range.

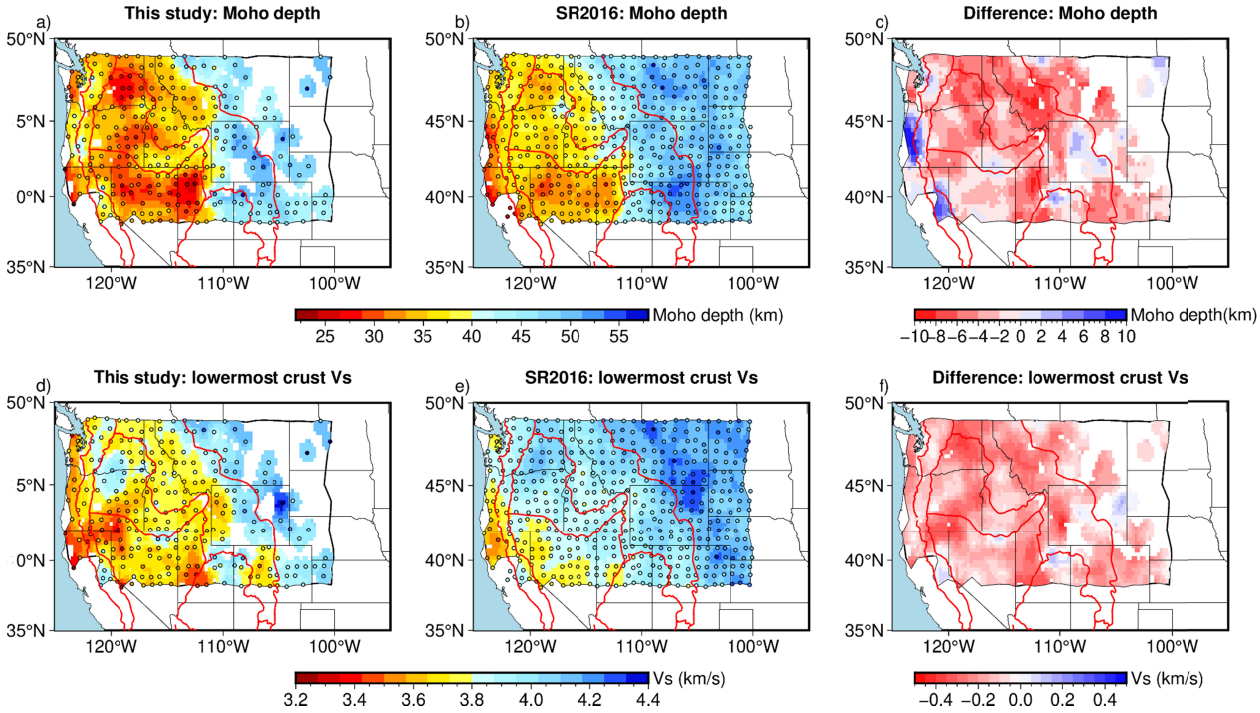

Figure 9. Comparison of Moho depth (**a-c**) and lowermost crust Vs (**d-f**) with SR2016 model. Panels from the left column to the right column are the results of this study, the SR2016 model, and the difference between them (This study – SR2016), respectively.

4.3 Other improvements and implications

Seismic attributes are influenced by various factors such as temperature, chemical composition, the presence of partial melting, or fluids. Therefore, conversely, seismic models can be used to infer these factors.

One notable feature in the Vp/Vs map is the high Vp/Vs ratios in the crystalline crust of coastal Oregon. The Vp/Vs ratios, ranging from ~ 1.85 to ~1.95, stand out as particularly high for crustal rocks (Christensen & Mooney, 1995). Several possible mechanisms may produce such elevated Vp/Vs ratios. These include: 1) mafic composition; 2) the existence of the cracks and fractures that lower the Vs; 3) the existence of fluid (e.g., melt) that lowers the Vs than to Vp; It has been speculated that this region might be accreted to the main continent during the early Eocene and may bear distinct crustal composition than other regions (Wells et al., 2014). Additionally, careful receiver function analysis has identified a layer bearing slab-bearing fluids at deep crustal depths that might be the subducted oceanic crust (Hansen et al., 2012). Vp/Vs ratios in such a layer are estimated to be as high as ~ 2, which can significantly contribute to elevated bulk crustal Vp/Vs measurements.

The new Moho depth result also imparts some new insights. The observation of reduced crustal thickness beneath the Basin and Range region suggests a diminished contribution of crustal support to the topography through isostasy, indicative of greater dynamic support from the underlying mantle. Additionally, a stronger contrast in crustal thickness between Basin and Range and adjacent tectonic provinces such as Colorado Plateau also predicts greater Gravitational Potential Energy (GPE) differences (e.g., Bahadori et al., 2022), which leads to a different GPE-induced stress field.

Another improvement from the new approach is the uppermost mantle Vs. Uppermost mantle Vs can be used to infer the temperature and possible distribution of partial melting (e.g., Hansen et al., 2015; Porter & Reid, 2021). However, the depth-velocity trade-off of surface waves often leads to the correlation between uppermost mantle Vs and Moho depth, as demonstrated by the synthetic test in Section 2 (Fig 10a). Due to this significant trade-off, few studies utilize the topmost mantle Vs for mapping the Moho temperature. Instead, much research on mantle temperature focuses on a greater depth, where it is believed that the influence of crustal thickness uncertainties is relatively small (e.g., below 50 km in Rau & Forsyth, 2011). In studies related to Moho temperature, Pn velocity is often utilized (e.g., Boyd, 2020; Schutt et al., 2018). However, with the incorporation of H-κ stacked energy, the accepted model ensemble results in a greatly reduced trade-off between Moho depth and uppermost mantle Vs, and consequently, a better-constrained uppermost mantle Vs (Fig. 10a). In this synthetic test, the accepted models obtained through the new approach exhibit a 67% reduction in uppermost mantle Vs uncertainty (0.03 km/s) compared to the case without incorporating H-κ stacked energy (0.09 km/s, Fig. 10a). As a result, application of the new method to NW US yields an improved uppermost mantle image. As depicted in Fig.10b, the new model exhibits relatively faster Vs beneath the Columbia River Flood Basalt, northern Rocky Mountains, Wyoming Craton, and part of the Basin and Range. Slower uppermost mantle Vs is seen near the High Lava Plain, northeast of Basin and Range, the Yellowstone hotspot track, Modoc Plateau, and the Cascadia region. Compared to the SR2016 model (Fig. 10c), the new result shows a generally slower uppermost mantle Vs in the northwestern US, except in certain regions such as the northern Cascades, northern Sierra Nevada, southern Modoc Plateau, Wyoming Craton, and the northern margin of the Colorado Plateau.

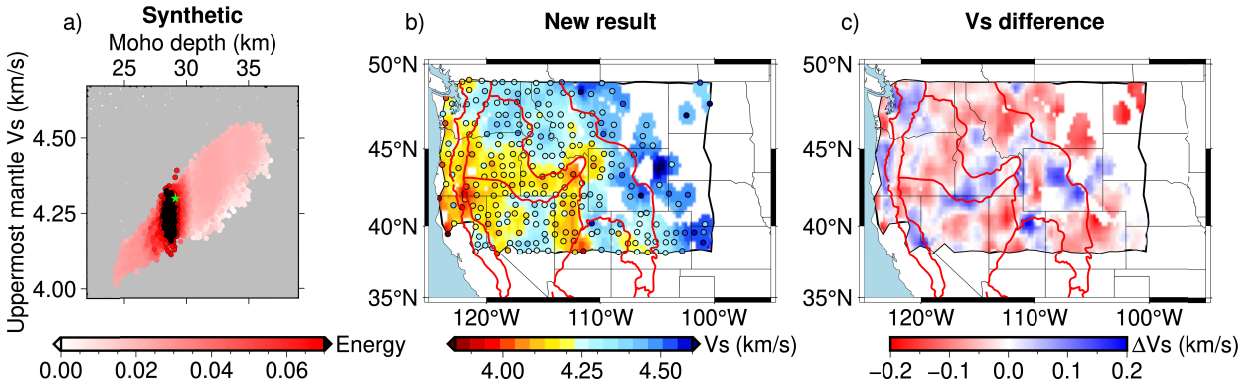

Figure 10. Improvements in uppermost mantle structures. **a**) Trade-off between Moho depth and uppermost mantle Vs (averaged Vs within 5 km below Moho), similar to Fig. 1a; **b**) Map view of uppermost mantle Vs of our new result; **c**) Map view of the differences (new result - SR2016) between our newly obtained uppermost mantle Vs and that of the SR2016 model.

Given that the trade-off between topmost mantle Vs and Moho depth has been reduced, the more accurate Vs has the potential to be used to constrain the Moho temperature, and the usage of Vs to constrain uppermost mantle temperature is no longer limited to depths much greater than Moho. In the new map, the overall variation is consistent with the Pn-derived Moho temperature map (Schutt et al., 2018) where the low Vs is found in regions with Moho temperature > 800 °C (e.g., Yellow stone hotspot track and Cascadia). In some places, discrepancies appear, e.g., the Wasatch Fault zone in central-West Utah, where the uppermost mantle Vs is low, but the Pn-derived Moho temperature is not high. However, the low Vs is consistent with the high geothermal heat flux in this area (Blackwell et al., 2011), indicating that the new Vs map provides a useful constraint to build future Moho temperature models.

4.4 Caveats of the work and potential refinements

The extraction of RFs was performed using the traditional time-domain iterative method, as described in section 3, without further processing. Also, the following quality control only removes some low-quality data but cannot solve the asymmetric problem caused by the interference of sediment-reverberations. One possible solution is to use higher-frequency RFs to separate the Moho-converted phases and sediment-reverberations since the low-velocity sedimentary layer can result in low-frequency reverberations. A more direct solution is to find a way of removing the sediment-reverberations from the RFs. Yu et al. (2015) proposed an approach to effectively remove the sediment reverberations and decipher the Moho-converted phases. If this approach can be applied to the RFs that we used in MC inversion, the asymmetric problem may be solved.

In this work, only the crystalline crust Vp/Vs is set as a free parameter, and the Vp/Vs ratio in the sedimentary layer is simply scaled from the Vs ratio (Brocher, 2005). One possible future improvement of the method is to perform the sedimentary-layer phases and reverberations in a sequential H-k stacking (e.g., Yeck et al., 2013) and include it in the joint MC inversion. Additionally, for the crystalline crust, only the bulk average Vp/Vs is resolved by the data, and it lacks depth sensitivity for investigating the deep crustal structure. The lower crust has been the center of the debate on the composition and evolution of the continental crust in general (e.g., Hacker et al., 2015b). To better understand its Vp/Vs ratio, it is thus important to incorporate additional constraints. Lin et al., (2012) and others have made observations of the Rayleigh wave local amplification and show that it provides additional sensitivity to the Vp and density that is different from the phase and group velocities or H/V ratios. If such data can be incorporated in the joint Monte Carlo inversion, additional sensitivity to the particular depth of the crust and possible resolution to the deep crustal structure (e.g., Vp/Vs or density) can be obtained.

4.5 Summary

In this paper, we present a novel method that incorporates the traditional H-κ stacking into the MC inversion of surface waves and receiver function waveforms to constrain the architecture of crust and uppermost mantle seismic structure. The feasibility of the new method is demonstrated by synthetic tests and further enhanced by the additional application to the USArray data in NW. US. We summarize our findings below:

1. The new approach greatly reduces the trade-offs between lowermost crust Vs, Moho depth, and bulk Vp/Vs ratio of the crystalline crust, eliminating the requirement of assuming crustal Vp/Vs in joint inversions and resulting in more accurate results.
2. In addition to crustal structures, the new approach also enhances the accuracy of upper mantle velocity structure by reducing the trade-off between Moho and upper mantle Vs.
3. Certain reverberations caused by thin sedimentary layers can contaminate the Moho-converted phases by introducing an apparent shift, leading to a mismatch between the maximum energy and the true arrival time. In such cases, the results may introduce bias, primarily affecting the estimation of Vs and Moho depth.
4. When the sedimentary layer is thick enough, some reverberations generated by this sedimentary layer are sufficiently separated from the Moho-converted phases to the extent that there is no energy shift, but the Moho-converted phases are still affected to the point of asymmetry. As a result, there exists a small bias in the obtained result, but much lower than that caused by the apparent maximum energy shift due to sediment contamination.
5. After applying the new method to ~ 450 USArray stations in NW US, map views of the key crustal parameters (i.e., lowermost crust Vs, Moho depth, and bulk Vp/Vs of crystalline crust) show general consistency with some previous studies but also reveals additional new features.
6. The noticeable high Vp/Vs ratios in the crystalline crust of coastal Oregon suggest the possible presence of mafic composition or the existence of fluid or cracks.
7. The new Moho depth result suggests reduced crustal support in the Basin and Range region, with greater dynamic mantle support and significant Gravitational Potential Energy differences compared to adjacent tectonic provinces.
8. The uppermost mantle Vs (averaged within 5 km below the Moho) map exhibits good consistency with the Moho temperature map derived from Pn velocity, providing new potential for using Vs to constrain the Moho temperature and crustal thermal properties.

Looking forward, through improved data processing techniques (e.g., removing sediment-related reverberations), the issue of the maximum energy shift present in this new approach may be resolved. Moreover, by incorporating other observables (e.g., local amplification data), the depth resolution for Vp/Vs can be further enhanced, thereby obtaining more accurate deep crustal structures. More accurate seismic structures, in turn, can offer valuable implications in other

areas of Earth science. These potential improvements warrant future investigations after the initial effort summarized in this paper.

Acknowledgments

The authors thank William Holt for his valuable discussions. The authors also thank Xiaofei Ma and Anthony R. Lowry for providing the U.S. continental Vp/Vs ratios. The work is mostly supported by NSF OPP-1945856, EAR-2322632. Aspects of the work were also supported by SCEC-21177, EAR-2317868, and OPP-2145410. The facilities of EarthScope Consortium were used for access to waveforms, related metadata, and derived products used in this study. These services are funded through the Seismological Facility for the Advancement of Geoscience (SAGE) Award of the National Science Foundation under Cooperative Support Agreement EAR-1851048. The authors also appreciate two anonymous reviewers and the associate editor of GRL who contributed their expertise, time, and invaluable insights to enhance the quality of this paper.

Open Research

The seismic data (including raw data for both surface wave observables and receiver functions) are downloaded from Incorporated Research Institutions for Seismology (IRIS, http://ds.iris.edu/ds/nodes/dmc/data/). The Vp/Vs ratios of Earthscope Automated Receiver Survey (EARS) are downloaded from IRIS (http://ds.iris.edu/ds/products/ears/#TOOLS) The three key parameters of each station in our study can be found in the supplemental material. The seismic model is scheduled to be available to the public at Earthscope Earth Model Collaborations (https://ds.iris.edu/ds/products/emc-earthmodels/) after the manuscript is published.

590

591 ## References

592 Ammon, C. J., Randall, G. E., & Zandt, G. (1990). On the nonuniqueness of receiver function inversions. *Journal of*
593 *Geophysical Research*, *95*(B10). https://doi.org/10.1029/jb095ib10p15303
594 Bahadori, A., Holt, W. E., Austermann, J., Campbell, L., Rasbury, E. T., Davis, D. M., Calvelage, C. M., & Flesch,
595 L. M. (2022). The role of gravitational body forces in the development of metamorphic core complexes.
596 *Nature Communications*, *13*(1). https://doi.org/10.1038/s41467-022-33361-2
597 Blackwell, D., Richards, M., Frone, Z., Batir, J., Ruzo, A., Dingwall, R., & Williams, M. (2011, October 24).
598 *Temperature-At-Depth Maps For the Conterminous US and Geothermal Resource Estimates*.
599 Boyd, O. S. (2020). *Temperature Model in Support of the U.S. Geological Survey National Crustal Model for*
600 *Seismic Hazard Studies*. https://doi.org/10.3133/ofr20191121
601 Brocher, T. M. (2005). Empirical relations between elastic wavespeeds and density in the Earth's crust. *Bulletin of*
602 *the Seismological Society of America*, *95*(6), 2081–2092. https://doi.org/10.1785/0120050077
603 Chen, Y., & Niu, F. (2013). Ray-parameter based stacking and enhanced pre-conditioning for stable inversion of
604 receiver function data. *Geophysical Journal International*, *194*(3), 1682–1700.
605 https://doi.org/10.1093/gji/ggt179
606 Christensen, N. I., & Mooney, W. D. (1995). Seismic velocity structure and composition of the continental crust: a
607 global view. *Journal of Geophysical Research*, *100*(B6), 9761–9788. https://doi.org/10.1029/95JB00259
608 Crotwell, H. P., & Owens, T. J. (2015). *Automated Receiver Function Processing*. http://www.seis.sc.edu/ears/.
609 Delph, J. R., Levander, A., & Niu, F. (2018). Fluid Controls on the Heterogeneous Seismic Characteristics of the
610 Cascadia Margin. *Geophysical Research Letters*, *45*(20), 11,021-11,029.
611 https://doi.org/10.1029/2018GL079518
612 Eagar, K. C., Fouch, M. J., James, D. E., & Carlson, R. W. (2011). Crustal structure beneath the High Lava Plains of
613 eastern Oregon and surrounding regions from receiver function analysis. *Journal of Geophysical Research:*
614 *Solid Earth*, *116*(2). https://doi.org/10.1029/2010JB007795
615 Hacker, B. R., & Abers, G. A. (2004). Subduction Factory 3: An Excel worksheet and macro for calculating the
616 densities, seismic wave speeds, and H2O contents of minerals and rocks at pressure and temperature.
617 *Geochemistry, Geophysics, Geosystems*, *5*(1). https://doi.org/10.1029/2003GC000614
618 Hacker, B. R., Kelemen, P. B., & Behn, M. D. (2015a). Continental lower crust. *Annual Review of Earth and*
619 *Planetary Sciences*, *43*, 167–205. https://doi.org/10.1146/annurev-earth-050212-124117
620 Hacker, B. R., Kelemen, P. B., & Behn, M. D. (2015b). Continental lower crust. *Annual Review of Earth and*
621 *Planetary Sciences*, *43*, 167–205. https://doi.org/10.1146/annurev-earth-050212-124117
622 Hansen, R. T. J., Bostock, M. G., & Christensen, N. I. (2012). Nature of the low velocity zone in Cascadia from
623 receiver function waveform inversion. *Earth and Planetary Science Letters*, *337–338*, 25–38.
624 https://doi.org/10.1016/j.epsl.2012.05.031
625 Hansen, S. M., Dueker, K., & Schmandt, B. (2015). Thermal classification of lithospheric discontinuities beneath
626 USArray. *Earth and Planetary Science Letters*, *431*, 36–47. https://doi.org/10.1016/j.epsl.2015.09.009
627 He, L., Guo, Z., Chen, Y. J., Huang, Q., & Yang, Y. (2021). Seismic Imaging of a Magma Chamber and Melt
628 Recharge of the Dormant Datong Volcanoes. *Earth and Space Science*, *8*(12).
629 https://doi.org/10.1029/2021EA001931
630 Juliá, J., Ammon, C. J., Herrmann, R. B., & Correig, A. M. (2000). Joint inversion of receiver function and surface
631 wave dispersion observations. *Geophysical Journal International*, *143*(1), 99–112.
632 https://doi.org/https://doi.org/10.1046/j.1365-246x.2000.00217.x
633 Langston, C. A. (1977). CORVALLIS, OREGON, CRUSTAL AND UPPER MANTLE RECEIVER STRUCTURE
634 FROM TELESEISMIC P AND S WAVES. In *Bulletin of the Seismological Society of America* (Vol. 67, Issue
635 3). http://pubs.geoscienceworld.org/ssa/bssa/article-pdf/67/3/713/5320727/bssa0670030713.pdf
636 Ligorría, J. P., & Ammon, C. J. (1999). Iterative Deconvolution and Receiver-Function Estimation. In *Bulletin of the*
637 *Seismological Society of America* (Vol. 89).
638 Lin, F. C., Tsai, V. C., & Ritzwoller, M. H. (2012). The local amplification of surface waves: A new observable to
639 constrain elastic velocities, density, and anelastic attenuation. *Journal of Geophysical Research: Solid Earth*,
640 *117*(6). https://doi.org/10.1029/2012JB009208
641 Lowry, A. R., & Pérez-Gussinyé, M. (2011). The role of crustal quartz in controlling Cordilleran deformation.
642 *Nature*, *471*(7338), 353–359. https://doi.org/10.1038/nature09912

643 Ma, X., & Lowry, A. R. (2017). USArray Imaging of Continental Crust in the Conterminous United States.
644 *Tectonics*, *36*(12), 2882–2902. https://doi.org/10.1002/2017TC004540
645 Porter, R., & Reid, M. (2021). Mapping the Thermal Lithosphere and Melting Across the Continental US. In
646 *Geophysical Research Letters* (Vol. 48, Issue 7). Blackwell Publishing Ltd.
647 https://doi.org/10.1029/2020GL092197
648 Rau, C. J., & Forsyth, D. W. (2011). Melt in the mantle beneath the amagmatic zone, Southern Nevada. *Geology*,
649 *39*(10), 975–978. https://doi.org/10.1130/G32179.1
650 Ritzwoller, M. H., Lin, F.-C., & Shen, W. (2011). Ambient noise tomography with a large seismic array. *Comptes*
651 *Rendus Geoscience*, *343*(8–9), 558–570.
652 Schmandt, B., Jiang, C., & Farrell, J. (2019). Seismic perspectives from the western U.S. on magma reservoirs
653 underlying large silicic calderas. In *Journal of Volcanology and Geothermal Research* (Vol. 384, pp. 158–
654 178). Elsevier B.V. https://doi.org/10.1016/j.jvolgeores.2019.07.015
655 Schmandt, B., Lin, F. C., & Karlstrom, K. E. (2015). Distinct crustal isostasy trends east and west of the Rocky
656 Mountain Front. *Geophysical Research Letters*, *42*(23), 10290–10298. https://doi.org/10.1002/2015GL066593
657 Schutt, D. L., Lowry, A. R., & Buehler, J. S. (2018). Moho temperature and mobility of lower crust in the western
658 United States. *Geology*, *46*(3), 219–222. https://doi.org/10.1130/G39507.1
659 Shen, W., & Ritzwoller, M. H. (2016). Crustal and uppermost mantle structure beneath the United States. *Journal of*
660 *Geophysical Research: Solid Earth*, *121*(6), 4306–4342. https://doi.org/10.1002/2016JB012887
661 Shen, W., Ritzwoller, M. H., & Schulte-Pelkum, V. (2013). A 3-D model of the crust and uppermost mantle beneath
662 the Central and Western US by joint inversion of receiver functions and surface wave dispersion. *Journal of*
663 *Geophysical Research: Solid Earth*, *118*(1), 262–276. https://doi.org/10.1029/2012JB009602
664 Shen, W., Ritzwoller, M. H., Schulte-Pelkum, V., & Lin, F. C. (2013). Joint inversion of surface wave dispersion
665 and receiver functions: A Bayesianmonte-Carlo approach. *Geophysical Journal International*, *192*(2), 807–
666 836. https://doi.org/10.1093/gji/ggs050
667 Sui, S., Shen, W., Mahan, K., & Schulte-Pelkum, V. (2022). Constraining the crustal composition of the continental
668 U.S. using seismic observables. *GSA Bulletin*. https://doi.org/10.1130/b36229.1
669 Trabant, C., Hutko, A. R., Bahavar, M., Karstens, R., Ahern, T., & Aster, R. (2012). Data products at the IRIS
670 DMC: Stepping stones for research and other applications. *Seismological Research Letters*, *83*(5), 846–854.
671 https://doi.org/10.1785/0220120032
672 Wells, R., Bukry, D., Friedman, R., Pyle, D., Duncan, R., Haeussler, P., & Wooden, J. (2014). Geologic history of
673 Siletzia, a large igneous province in the Oregon and Washington Coast Range: Correlation to the geomagnetic
674 polarity time scale and implications for a long-lived Yellowstone hotspot. *Geosphere*, *10*(4), 692–719.
675 https://doi.org/10.1130/GES01018.1
676 Yang, Y., Yao, H., Wu, H., Zhang, P., & Wang, M. (2020). A new crustal shear-velocity model in Southwest China
677 from joint seismological inversion and its implications for regional crustal dynamics. *Geophysical Journal*
678 *International*, *220*(2), 1379–1393. https://doi.org/10.1093/gji/ggz514
679 Yeck, W. L., Sheehan, A. F., & Schulte-Pelkum, V. (2013). Sequential h-κ stacking to obtain accurate crustal
680 thicknesses beneath sedimentary basins. *Bulletin of the Seismological Society of America*, *103*(3), 2142–2150.
681 https://doi.org/10.1785/0120120290
682 Yu, Y., Song, J., Liu, K. H., & Gao, S. S. (2015). Determining crustal structure beneath seismic stations overlying a
683 low-velocity sedimentary layer using receiver functions. *Journal of Geophysical Research: Solid Earth*,
684 *120*(5), 3208–3218. https://doi.org/10.1002/2014JB011610
685 Zhu, L., & Kanamori, H. (2000). Moho depth variation in southern California from teleseismic receiver functions.
686 *Journal of Geophysical Research: Solid Earth*, *105*(B2), 2969–2980. https://doi.org/10.1029/1999jb900322
687